



CFD model of a methane fuelled single cell SOFC stack for analysing the combined effects of macro/micro structural parameters

Shahin Hosseini^a, Khaliq Ahmed^b, Moses O. Tadé^{a,*}

^a Centre for Process Systems Computations (CPSC), Department of Chemical Engineering, Curtin University, GPO Box U1987, Perth, WA 6845, Australia

^b Ceramic Fuel Cells Ltd., 170 Browns Road, Noble Park, Vic. 3174, Australia

H I G H L I G H T S

- Coupled CFD model of a direct internal reforming single cell SOFC stack is developed.
- Innovative technique is taken to accelerate finite volume treatment of the electrodes.
- The model is validated by comparison with experimental data from the same geometry.
- Interaction of the macro/micro structural parameters affects distribution of fields.
- Anode microstructures have different intensity effects on electro-chemical reactions.

A R T I C L E I N F O

Article history:

Received 9 October 2012

Received in revised form

16 December 2012

Accepted 17 December 2012

Available online 14 January 2013

Keywords:

Planar SOFC

CFD model

Anode microstructure

Diffusion layer

SOFC stack

A B S T R A C T

A fully coupled CFD model of a direct internal reforming single cell SOFC stack previously designed by Ceramic Fuel Cell Ltd (CFCL) has been developed. In this model, an innovative solution technique for accelerating finite volume treatment of the electrodes as two distinct layers, a diffusion layer and a catalyst layer, is taken to analyse the combined effects of the macro/microstructural parameters on distribution of fields and each of the reactions involved in the process. To assess the simulation results, the model is not only evaluated with the CFCL experimental data that was reported from the similar geometry, but it is also assessed for the effects of the reforming and water gas shift reactions. It is found that a 3D model is more representative of the global reforming reaction rate. Furthermore, distributions of the key parameters along different spatial domains disclose the complex interaction between the anode flow field design and microstructural parameters of the anode diffusion layer. In fact, an optimal set of the anode microstructure that promotes the reforming reaction rate will not automatically result in improved SOFC performance. The developed model is a powerful tool to study complex fuel cell related problems and to optimize fuel cells' structure.

Crown Copyright © 2013 Published by Elsevier B.V. All rights reserved.

1. Introduction

Solid oxide fuel cells (SOFCs) are potentially attractive electro-chemical reactors due to their high efficiency and fuel flexibility [1]. In addition, the SOFCs' basic components can be fabricated into a variety of configurations among them the planar-type SOFC is desirable for many applications due to its compactness and high power density [2,3]. However, their design and development progressed slower than the other types of fuel cells. This is because of different problems which are associated with the high operating temperature including the requirement for the high performance

materials, sealing problems and difficulties in thermal management [4]. In view of this, a promising alternative has been studied extensively to reduce the operating temperature by adopting anode supported structure in SOFC instead of the electrolyte layer support. For a thinner layer of the electrolyte film, SOFC can operate in a moderated temperature of 600–800 °C [4,5]. In addition, the commonly used Ni-based porous support provides internal reforming environment, which increases the applicability of the cell to methane-containing fuels without the need for converting methane to hydrogen in an external reformer [6]. Therefore, one of the important fields of the SOFC research is to explore the influences of the anode micro-characteristics on overall performance of the cell and the involved reactions. In this regards, mathematical modelling helps in reducing the need of the repetitive and costly experiments while amongst the models exist in the open literature,

* Corresponding author. Tel.: +61 8 9266 7581; fax: +61 8 9266 2681.

E-mail address: M.O.Tade@curtin.edu.au (M.O. Tadé).

macro and micro modelling approaches are the most common methods for treating the electrodes [5]. Essentially, in macro modelling approach, the reaction zones are assumed as the mathematical surfaces and treated as the boundary conditions [5]. This approach leads to less computational time and model complexity. Therefore, it is mostly applied in the cell and stack level models [4,7–12]. However, reforming reaction occurs within the anode electrode while the electrochemical reaction takes place at the electrode–electrolyte interface at TPB points with some extension of this zone into the bulk anode [13]. In view of this, some researchers attempted to use the micro modelling approach to model electrodes as the finite volumes of the electron–ion conducting particles scattered throughout the electrodes. For example, Hussain et al. [14] developed a 1D SOFC model to describe the multi-component species transport inside the porous anode. In that model, they assumed the variation of different parameters along the electrode's depth. In addition, water gas shift and electrochemical reactions were considered at two distinct layers of the anode electrode respectively. However, for accurate prediction of the cell performance, proper flow models with correct boundary conditions at the porous interface of the rib channels are required [15]. To meet this aim, multi-dimensional models are required. For example, Hussain et al. [13] extended their studies and developed a 2D PEN model of a planar SOFC in which the effect of the reforming reaction was included. In addition, the works reported by Shi and Xue [16,17], Anderson et al. [18] and Abbaspour et al. [19] are among the recent examples of the multi-dimensional models in which modellers attempted to implement the micro modelling approach. However, a challenge faced is that using this approach for a complete SOFC modelling, including complex interaction between the macro/micro structural parameters, multi-physics and electro-chemical reactions lead to highly complex descriptions, which are time consuming with respect to set up and simulation. Therefore, these models are effective in determining the performance of a single unit of a cell or electrode. In other words, none of the existing models of a single cell SOFC stack incorporate combined effects of the electrodes' microstructure and geometrical factors of the entire gas flow fields. As a result, in order to efficiently move towards cell and stack detailed models, it is very important to reduce computing requirements by adopting an easy and efficient modelling approach.

Building on the above mentioned studies, the purpose of this work is to develop a modified CFD model of an internal reforming single cell SOFC stack previously designed by Ceramic Fuel Cell Ltd. (CFCL). The uniqueness of this paper by the cell/stack level modelling approach is the implementation of the electrodes' microstructures in 3D model of a complete single cell SOFC stack. In fact, contrary to published work on SOFC modelling, determining the SOFC performance is not limited to a single unit of a cell or electrode while the combined effects of the electrodes'

microstructure and geometrical factors of the entire flow fields are considered simultaneously. Further advances are made for the volumetric treatment of the reactions involved in the process. In other words, compared to a common method in the published cell/stack modelling works, the effect of electro-chemical reactions are not reducing to the interface boundary conditions while they are treated as the volumetric source term of the coupled transport equations. However, to reduce the computational time and memory limitation, an innovative solution technique between the macro and micro modelling approach is taken. In this regard, the electrode catalyst layers are divided into a number of control volumes arranged in a single layer grid. To articulate the significance of the simulation results, it is worth mentioning that the predicted $V-I$ curves are evaluated from the experimental polarization data that was reported by CFCL and from the similar geometry. However, the model is not only evaluated by the overall polarization curves as it is usually done in the literature but also the simulation results are assessed for the reforming and water gas shift and in the absence of the electrochemical reactions. Finally, as the new insight to the practical application, different parameters are calculated from local conditions while parametric analysis is performed to investigate the effects of porosity, pore size and thickness of the anode diffusion layer on the distribution of fields and each of the reactions involved. To achieve these aims, only one variable is changed at a time while keeping the other variables constant.

2. Model geometry

Fig. 1 illustrates the computational domains of the planar SOFC proposed in this study. In this regard, the anode and cathode flow fields are the symmetrical half layer array of the SOFC stack consisting of two adjacent cells proposed by CFCL. In addition, the PEN structure (Positive electrode–Electrolyte–Negative electrode) was treated as the anode and cathode diffusion layers and a thin film of the electrolyte that is sandwiched between distinct anode and cathode catalyst layers. Similar to the approach considered by Joen [20] and Shi et al. [21], the porous electrodes are assumed to be homogeneous bimodal mixture of the electron and ion conducting particles with identical radius within each of the electrode domains. This matter facilitates incorporating of the anode microstructural parameters into the model of the SOFC stack and helps in quantitative design and optimization of the electrodes.

3. Model equations

Considering the computational time and accuracy of the simulation results, we need to make further assumptions to reduce the complexity of the model to a manageable level whilst preserving the salient features of the problem at hand. In this regard, fluids can

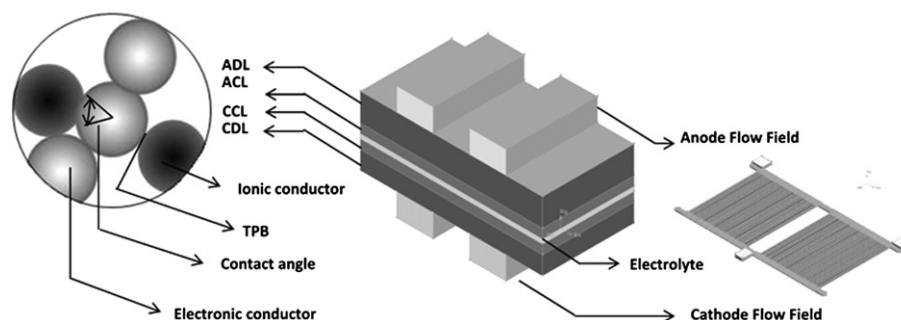


Fig. 1. Domain decomposition for a planar SOFC stack.

be modelled as incompressible-laminar flows due to small velocity and pressure gradients. Furthermore, with respect to the high temperature and moderate pressure, fuel and air gases can be thermodynamically modelled with the ideal gas assumption [22]. In view of this, heat capacity, viscosity and thermal conductivity of the gas mixtures are calculated with the ideal gas mixing law. In addition, focussing on the purpose of this study, we decided to use a general frame work based on the computational fluid dynamic (CFD) approach to solve the following conservation equations of continuity, momentum, energy and species. The steady state simulation results were obtained from the transient solution of the model since the results did not change after more than 1500 iterations for each case. Therefore, each equation is presented in a dynamic form. In this regard, the continuity and momentum equations are as follows:

$$\frac{\partial \rho}{\partial t} + \nabla(\rho \vec{u}) = 0 \quad (1)$$

$$\frac{\partial(\rho \vec{u})}{\partial t} + \nabla(\rho \vec{u} \vec{u}) = -\nabla P + \nabla(\tau) + \rho g + S_M \quad (2)$$

Inclusion of the additional source term S_M , allows the equation of motion to be valid for both the porous media and gas channels. In view of this, considering the laminar flow condition, the momentum source term can be calculated from the following equation that is based on the generalized Darcy's law. Here, μ is the viscosity; α_p – permeability; ε – Porosity; d_p – mean particle diameter and ι is tortuosity.

$$S_M = -\frac{\mu}{\alpha_p} \vec{u} \quad (3)$$

$$\alpha_p = \frac{\varepsilon^3 d_p^2}{72 \iota (1 - \varepsilon)^2} \quad (4)$$

Furthermore, it is known that the temperature distribution in SOFC strongly influences the cell performance. In view of this, the conservation of energy is computed from a porosity weighted composite of energy equations of the solid and fluid phases and can be expressed as Eq. (5). Here, E^f and E^s are the fluid and solid total energy respectively; ε is the porosity of the medium; k^{eff} is the effective thermal conductivity; and S_h includes the heat of the electro-chemical reactions. Table 1 provides the properties for different solid components of the cell.

$$\begin{aligned} \frac{\partial}{\partial t} \left(\varepsilon \rho^f E^f + (1 - \varepsilon) \rho^s E^s \right) + \nabla \cdot \left(v \left(\rho^f E^f + P \right) \right) \\ = \nabla \left[k^{\text{eff}} \text{grad}(T) - \left(\sum_i h_i J_i \right) + \left(\tau \cdot \vec{u} \right) \right] + S_h \end{aligned} \quad (5)$$

$$k^{\text{eff}} = \varepsilon k^f + (1 - \varepsilon) k^s \quad (6)$$

Table 1
Properties for different solid components of the cell [10].

Components	k^s (Wm ⁻¹ K ⁻¹)	ρ^s (kg m ⁻³)	c_p (kJ kg ⁻¹ ·K ⁻¹)
Anode	6.23	7000	0.65
Cathode	9.6	5620	0.9
Electrolyte	2.7	5560	0.3
Interconnect	13	7700	0.8

The species transport equation is defined as the following forms. Here, J_i represents the diffusive flux of each component; D_i^{eff} and D_i^T are the reactants' mass and thermal diffusion coefficients; and $(S_i^r)_{\text{overall}}$ is the species mass source term from N_R reactions. To calculate the effective diffusion coefficients, the contribution of the molecular and Knudsen diffusivities was considered (cf. – Appendix A).

$$\frac{\partial \rho_i}{\partial t} = -(\nabla \cdot \rho_i \vec{u}) - M_{w,i} (\nabla \cdot J_i + (S_i^r)_{\text{overall}}) \quad (7)$$

$$J_i = -\sum \nabla \left(\rho_{i,\text{mol}} D_i^{\text{eff}} \right) - D_i^T \frac{\nabla T}{T} \quad (8)$$

$$(S_i^r)_{\text{overall}} = \sum_{\ell=1}^{N_R} (S_i^r)_{\ell} \quad (9)$$

4. Reaction source terms

4.1. Chemical reaction

Three dimensional simulation involving a complete set of elementary reactions would be difficult to converge and will be computationally expensive. Therefore, in this study, we considered the overall reforming and water gas shift reactions as follows:



Although in some SOFC models the reforming reaction was assumed under thermodynamic equilibrium [23,24], a more correct model is based on the kinetic approach [25]. In this regard, different papers have focused on the kinetics of the steam reforming of nickel-based anode material. However, SOFC anode manufacturing processes are different from the conventional catalyst preparation techniques. Therefore, in this work, the steam reforming reaction was determined in the anode diffusion layer (ADL) using a kinetic model developed by Ahmed and Foger [26] (Eq. (12)). The salient feature of this model is that, it was developed from the data that were collected on 50 μm thick anodes screen-printed on 100 μm zirconia electrolyte, which is representative of the anode of planar electrolyte-supported SOFCs. Nevertheless, as far as kinetics is concerned it is equally applicable to the reforming layer of anode supported SOFCs.

$$S_r^{\text{SMR}} = A_s^{\text{expose}} \cdot P_{\text{CH}_4}^{0.85} \cdot P_{\text{H}_2\text{O}}^{-0.35} \cdot \exp\left(-\frac{E_{\text{cat}}}{RT}\right) \quad (12)$$

For the water gas shift reaction, again different approaches can be found in the literature: global reaction mechanism that considers reaction in the anode only [27,28], global reaction mechanism that considers reaction in the anode and in the fuel gas channels [29], and a more advanced reaction mechanism that includes catalytic surface reaction kinetics for steam reforming, water–gas shift reaction and the Boudouard mechanism [30]. In this study, water-gas shift reaction was considered in both anode electrode and fuel gas channels by the following equilibrium limited rate expression [31].

$$S_r^{\text{WGS}} = \kappa_f^{\text{WGS}} \left(P_{\text{H}_2\text{O}} P_{\text{CO}} - \frac{P_{\text{H}_2} P_{\text{CO}_2}}{k_{\text{eq}}^{\text{WGS}}} \right) \quad (13)$$

In the above equation, temperature dependent expression for κ_f^{WGS} was deduced from Arrhenius fit of Lehnert's data [32], and the equilibrium constant $k_{\text{eq}}^{\text{WGS}}$ was taken from the literature [33].

$$\kappa_f^{\text{WGS}} = 0.0171 \exp\left(-\frac{103,191}{RT}\right) \quad (14)$$

$$\kappa_{\text{eq}}^{\text{WGS}} = 1.767 \times 10^{-2} \exp(4400/T) \quad (15)$$

The molar rates of production or consumption of various species in the anode diffusion layer can be formulated as follows.

$$(S_{\text{CH}_4}^r)^{\text{Chem}} = -S_r^{\text{SMR}} \quad (16)$$

$$(S_{\text{CO}}^r)^{\text{Chem}} = S_r^{\text{SMR}} - S_r^{\text{WGS}} \quad (17)$$

$$(S_{\text{H}_2\text{O}}^r)^{\text{Chem}} = -S_r^{\text{SMR}} - S_r^{\text{WGS}} \quad (18)$$

$$(S_{\text{H}_2}^r)^{\text{Chem}} = 3S_r^{\text{SMR}} + S_r^{\text{WGS}} \quad (19)$$

$$(S_{\text{CO}_2}^r)^{\text{Chem}} = S_r^{\text{WGS}} \quad (20)$$

In addition, the heat effect from chemical reactions is introduced as the volumetric source term into the equation of energy.

$$S_h^{\text{Chem}} = - \sum_i h_i (S_i^r)^{\text{Chem}} \quad (21)$$

4.2. Electrochemical reaction

In the model geometry of this work, TPBs within the electrode catalyst layers were treated as the finite volumes with thickness of 20 μm . However, to reduce the computational time and the model complexity, the electrode catalyst layers were divided into a number of control volumes arranged in a single layer grid. In this way, assuming the electrolyte layer as the sole contributor to the ohmic losses, the equivalent circuit approach was employed to solve the electrochemical sub-model together with all transport equations within the catalyst layers. In view of this, the effects from the electrochemical reaction were treated as the heat and mass source terms in the governing equations and can be calculated as S_h^{elec} and $(S_i^r)^{\text{elec}}$ respectively [34].

$$(S_i^r)^{\text{elec}} = \frac{A_s^{\text{contact}} \cdot \nu_i \cdot i_{\text{cell}}}{nF} \quad (i = \text{H}_2, \text{H}_2\text{O} \text{ and } \text{O}_2) \quad (22)$$

$$S_h^{\text{elec}} = A_s^{\text{contact}} \cdot i_{\text{cell}} \left(\frac{\Delta H^{\text{elec}}}{2F} - E_{\text{cell}} \right) \quad (23)$$

Here, A_s^{contact} is the specific contact surface area for the electrochemical reaction; E_{cell} is the cell voltage; ΔH^{elec} is the enthalpy of the electrochemical reaction; and i_{cell} is the cell current density that is obtained from the voltage equation [9].

$$i_{\text{cell}} = (E_{\text{OCV}} - E_{\text{cell}} - \eta_{\text{act}}^A - |\eta_{\text{act}}^C|) / R_{\text{Ohmic}} \quad (24)$$

$$R_{\text{Ohmic}} = \frac{\ell_A}{\partial_A} + \frac{\ell_{\text{elyt}}}{\partial_{\text{elyt}}} + \frac{\ell_C}{\partial_C} \quad (25)$$

$$\partial_A = 9 \times 10^7 e^{-\left(\frac{1150}{T}\right)} \quad (26)$$

$$\partial_C = 4 \times 10^7 e^{-\left(\frac{1200}{T}\right)} \quad (27)$$

$$\partial_{\text{elyt}} = 3.34 \times 10^4 e^{-\left(\frac{10,300}{T}\right)} \quad (28)$$

As it comes from the above mentioned correlations [7,35], the electrolyte resistance is the main contributor to the overall ohmic resistance of the cell that is calculated from a temperature dependant expression (Eq. (28)). Additionally, $\eta_{\text{act}}^{A/C}$ are the anode/cathode activation overpotentials; and E_{OCV} is the open circuit voltage, which is calculated from the Butler–Volmer and the Nernst equations respectively. As it is shown below, the concentration overpotentials are implicitly included in the Nernst equation, considering that the species molar fractions and temperature in Eqs. (29) and (30) were evaluated at the electrode catalyst layers [36,37]. Additionally, considering the air flow that is about 6 times higher than the fuel flow, oxygen is in the excess amount so that the variation of its partial pressure within the air gas channels can be neglected. In view of this, the flux boundary condition estimates the oxygen molar fraction at the cathode catalyst layer. This is similar to the approach suggested by Danilov and Tade [9].

$$E_{\text{OCV}} = \frac{\Delta G_{\text{H}_2/\text{O}_2}}{2F} + \frac{RT}{2F} \ln \left(\frac{(y_{\text{O}_2}^{\text{CCL}})^{0.5} y_{\text{H}_2}^{\text{ACL}}}{y_{\text{H}_2}^{\text{ACL}}} \right) \quad (29)$$

$$\eta_{\text{act}}^{A/C} = \frac{2RT}{n_e F} \sinh^{-1} \left(\frac{i_{\text{cell}}}{2i_0^{A/C}} \right) \quad (30)$$

Furthermore, assuming the electrode porous media as a binary mixture of the monotonic spherical electron and ion conducting particles, the statistical properties including the mean particle diameter d_p , and the pore radius r_p can be estimated as follows:

$$\frac{1}{d_p} = \frac{\psi_{\text{elde}}}{2r_{\text{elde}}} + \frac{\psi_{\text{elyt}}}{2r_{\text{elyt}}} \quad (31)$$

$$r_p = \frac{\varepsilon d_p}{3(1 - \varepsilon)} \quad (32)$$

Although the volumetric grain boundary between the ionic and electronic particles (TPB length) is given by Costamagna et al. [38], similar to many other researchers [13,16], this equation is used for estimating the volumetric surface area within the electrode catalyst layers.

$$A_s^{\text{contact}} = \pi \sin^2 \theta \cdot r_{\text{elde}}^2 n_t n_{\text{elde}} n_{\text{elyt}} \frac{Z_{\text{elde}} Z_{\text{elyt}}}{Z} P_{\text{elde}} P_{\text{elyt}} \quad (33)$$

In the above equations, ψ_{elde} and ψ_{elyt} are the electrode and electrolyte volume fractions in the anode porous media respectively; r_{elde} and r_{elyt} are the radius of the electrode and electrolyte particles correspondingly; θ is the contact angle between the electrode and electrolyte particles in the reactive volume; n_t is the total number of particles per unit of the reactive volume; n_{elde} and n_{elyt} are the number fractions of the electrode and electrolyte particles in the reactive volume respectively; Z_{elde} and Z_{elyt} are the coordination numbers of the electrode and electrolyte; P_{elde} and P_{elyt} are the probabilities of the electrode and electrolyte particles and finally Z is the total average coordination number, equal to 6. All

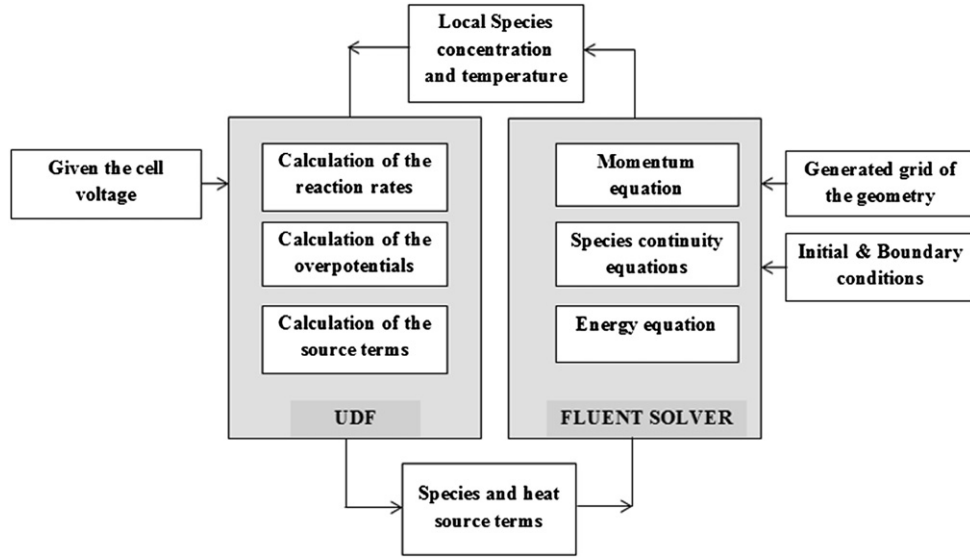


Fig. 2. schematic of the solution technique.

these parameters can be calculated by the following expressions [13]:

$$n_t = \frac{1 - \varepsilon}{(4/3)\pi r_{elde}^3 [n_{elde} + (1 - n_{elde})(r_{elyt}/r_{elde})^3]} \quad (34)$$

$$n_{elde} = \frac{\psi_{elde}}{[\psi_{elde} + ((1 - \psi_{elde})/(r_{elde}/r_{elyt})^3)]} \quad (35)$$

$$Z_{elde} = 3 + \frac{Z - 3}{[n_{elde} + (1 - n_{elde})(r_{elyt}/r_{elde})^2]} \quad (36)$$

$$Z_{elyt} = 3 + \frac{(Z - 3)(r_{elyt}/r_{elde})^2}{[n_{elde} + (1 - n_{elde})(r_{elyt}/r_{elde})^2]} \quad (37)$$

$$P_{elde} = \left[1 - \left(2 - \frac{Z_{elde} - elde}{2} \right)^{2.5} \right]^{0.4} \quad (38)$$

$$P_{elyt} = \left[1 - \left(2 - \frac{Z_{elyt} - elyt}{2} \right)^{2.5} \right]^{0.4} \quad (39)$$

However, for the reforming reaction, the specific surface area of the anode diffusion layer is defined as the total area exposed by the particles to the gas phase per unit of the reactive volume. For calculating the exposed surface area, the overlapping regions (contact specific area) should be reduced from the total surface of the rigid particles.

$$A_s^{\text{expose}} = A_s^{\text{rigid}} - A_s^{\text{contact}} \quad (40)$$

$$A_s^{\text{rigid}} = \frac{6(1 - \varepsilon)}{d_p} \quad (41)$$

However, as reported by Bertei and Nicoletta [39], neglecting the fraction of the surface lost in contacts, the exposed surface area is

overestimated in the order of 11.4% in the worst case for a binary mixture of the mono sized particles.

5. Numerical approach

There are several commercial packages for CFD analysis; however, in this work all the governing equations were solved in ANSYS (version 13.0) using the FLUENT solver. Considering the computational time and solution algorithm, Green-Gauss Cell Based method is selected for diffusion and 2nd order up-wind discretization scheme is selected for calculating the convection terms of each governing equation. For the iterative calculation of the pressure and velocity, FLUENT provides different algorithms; however, as suggested by Versteeg and Malalasekera [40], SIMPLE method is selected for implicit time treatment of the flow variables. Although all transport equations are solved in commercial FLUENT solver; however, it is linked with a user defined function (UDF) programmed by VC++ for implementing chemical and electrochemical reaction rates and calculating source terms of the governing equations. Fig. 2 presents the schematic of the solution technique and interaction between the FLUENT and user defined function (UDF). However, considering different aims as summarized in Table 2, numerical simulation was performed for three different cases.

6. Initial and boundary conditions

To initialize the numerical solution, we patched different values of the velocities, temperature and species concentration into different computational domains. Therefore, for the fuel and air gas

Table 2
Aims for different simulation cases.

Case No.	Aims
1	Analysis of pressure and velocity profiles for the anode flow field design
2	Analysis of the combined effects of the geometrical factors, micro structural parameters and catalytic chemical reactions on temperature and species concentration distribution
3	Expanding case 2 to include heat effects of the air flow and electrochemical reaction rate

Table 3
Inlet operating conditions.

Parameters	Anode side	Cathode side
Pressure (bar)	1	1
Temperature (K)	973 ~ 1023	973 ~ 1023
CH ₄ (%mole)	25.66	—
H ₂ (% mole)	15.31	—
CO ₂ (% mole)	5.08	—
CO (%mole)	0.098	—
H ₂ O (%mole)	53.47	—
N ₂ (%mole)	0.38	79
O ₂ (%mole)	0	21
Fuel flow (SLM)	Low Flow (LF): 0.067 (dry gas) and 0.073 (steam) High Flow (HF): 0.127 (dry gas) and 0.139 (steam)	—
Air flow (SLM)	—	0.8

Table 4
Model parameters [4,13,35].

Parameters	Values
Channel length (mm)	70
Channel width (mm)	1
Channel height (mm)	0.45
No. of channels	30
Thickness of the catalyst layers (μm)	20
Thickness of the diffusion layers (μm)	200
Electrolyte thickness (μm)	10
ACL porosity	0.4
ACL pore size (μm)	2.0
Volume fractions of the electrode/electrolyte particles	0.5
Contact angle between electrode/electrolyte particles (°)	15

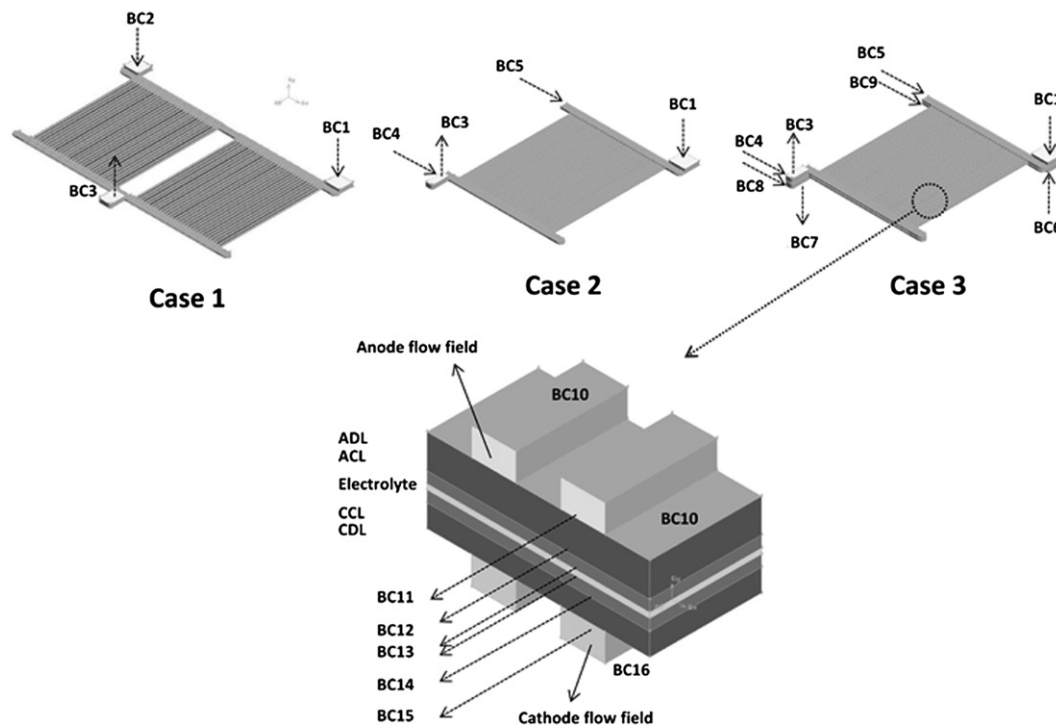
channels and electrode porous media, different flow variables were initialized relevant to their inlet values specified at the fuel and air inlet manifolds. For the solid electrolyte, which is impermeable to the reactants, initial values for the species concentration were set to

Table 5
Computational domains and the required boundary conditions for different cases.

Case No.	Computational domains	Internal boundaries	External boundaries
1	Fuel gas flow fields of two adjacent cells	N/A	BC1, BC2, BC3, BC10 and BC11
2	Fuel gas flow field for a single cell + ADL	BC11	BC1, BC3, BC4, BC5, BC10 and BC12
3	Complete cell including fuel flow field, ADL, ACL, Electrolyte, CCL, CDL and air flow field	BC11 ~ BC15	BC1, BC3, BC4, BC5, BC6, BC7, BC8, BC9, BC10 and BC16

zero and temperature can be set as the values from the fuel or air inlet condition. The inlet operating conditions and parameters used for the developed model can be found in [Tables 3 and 4](#), respectively.

However, in order to complete the model formulation, boundary conditions at different locations are required. In addition, due to interdependent transport processes in different components of an SOFC, the definition of boundary conditions involved both external and internal boundaries. In this regard, the locations of different boundaries are illustrated in [Fig. 3](#). Furthermore, for each case, the boundaries relevant to the computational domains are summarized in [Table 5](#). The external inlet boundaries (BC1, BC2, BC6), are set as the values for the inlet operating conditions and specified as the mass flow inlet to match the prescribed mass flow rates. At the outlet manifolds (BC3 and BC7), the pressure outlet boundary condition is adopted. Furthermore, as it is shown in [Fig. 3](#), for all cases, the computational domains only includes the land portion of interconnects; therefore, at external boundaries BC10 and BC16, thermal insulation and impermeable condition for the species transport are specified. Considering the simulation results from case 1, which is shown in [Fig. 4](#), there are symmetrical pressure and velocity profiles between two adjacent cells. Therefore, to speed up the computational time, for other cases we specified the symmetrical conditions at the boundaries BC4, BC5, BC8 and BC9.

**Fig. 3.** Illustration of locations at which boundary conditions are required in CFD model and for different cases.

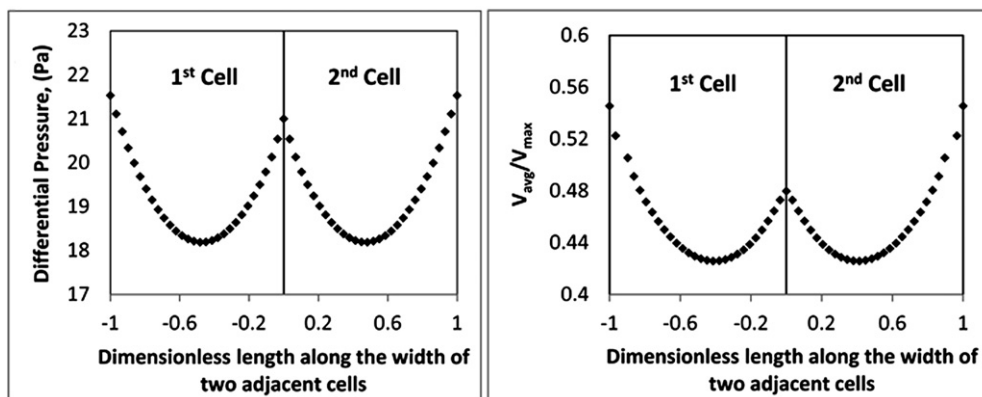


Fig. 4. Effects of flow field design on pressure and velocity profiles [6].

With respect to the internal boundaries, BC11 and BC15 represent the interfaces between the gas channels and electrode diffusion layers. However, for case 1, diffusion layers are not considered and then these two boundaries are specified as the impermeable wall with thermal insulating condition. For other cases, electrode functional layers are set for the porous media; therefore, the internal boundaries including BC11, BC12, BC14 and BC15 are specified as the interior faces which allows coupling the momentum, energy and species transfer equations. Therefore, varying boundary conditions for different operating variables are specified at these internal boundaries. Finally, with respect to the boundaries between the electrodes and electrolyte (BC13), the adjacent computational domains are coupled to account for the heat effects and zero species diffusion fluxes are specified on these stationary boundaries.

7. Simulation results and discussion

Two aspects that characterise a successful CFD simulation results are convergence and grid independency. For the converged solution, the residual convergence was limited to 10^{-6} for all variables followed by setting the solver on transient mode to confirm that the solution no longer changes with more iteration. Additionally, although the larger the number of cells the better the solution accuracy, the cost in terms of necessary computer hardware and calculation time depends on the fineness of the computational grid. As it is shown in Fig. 4, simulation results for case 1 depicts a symmetrical boundary condition between two adjacent cells. In view of this, a significant reduction in computational grid was achieved and to find the optimum grid density, simulation of case two was repeated for different grid densities. In this regards, a non-uniform computational grid with 470,490 cells is detailed enough for accurately calculating the reactions and

transport phenomena within the anode diffusion layer and their consequences on distribution of the key parameters along different special domains.

7.1. Model validation

As mentioned earlier, to assess the simulation results, the model is not only validated with the overall polarization curve as it is usually done in the open literature, but the model predictions are also evaluated for the effects of the reforming and water gas shift without including the electrochemical reactions. The simulation results are evaluated for the two cases cited above. In this regard, Table 6 shows the evaluation of the simulation results for case 2 obtained from different kinetic models [26,41], thermodynamic equilibrium data based on Gibbs free energy minimization method [42] and simulation results from CFCL 1D model. Although predictions from both 1D and 3D models closely approach thermodynamic equilibrium, 3D simulation shows that flow distribution effects resulting from the flow field design and, the finite external mass transfer within the gas distribution channels lead to a lowering percentage of methane conversion. In other words, the 1D model somewhat overpredicts conversion that would be achieved in a real geometry and the 3D model is more representative of the global reaction rate. This is exactly in line with the kinetics-based theories which assume that the reforming reaction is slow and

Table 6
Evaluation for 3D simulation results from case 2 (porosity = 0.4, pore size = 4.4 μm and inlet temperature = 1023).

	Equilibrium data (Gibbs Min. Meth.[42])	CFCL 1D model (Ahmed kinetic [26])	CFD model (Ahmed kinetic [26])	CFD model (Achenbach kinetic [41])
Outlet CH ₄ (%mole)	0.1789	0.1890	0.2033	0.1929
Outlet H ₂ (%mole)	0.3037	0.2807	0.2147	0.2342
Outlet temp. (K)	749	737	786	723
CH ₄ conversion (%)	32	30	24.7	28.6

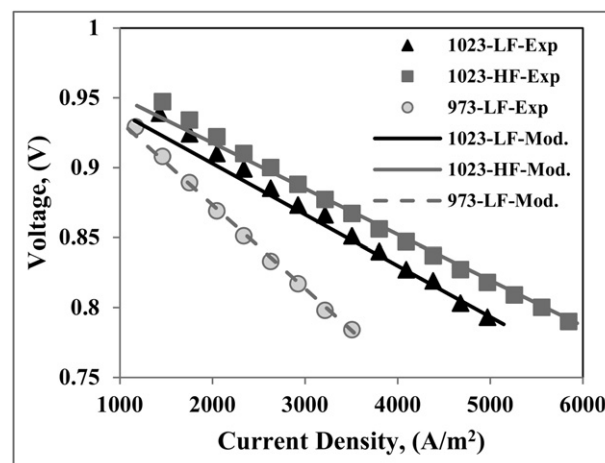


Fig. 5. Comparison of the predicted $V-I$ curves from CFD model with experimental data of the same geometry reported by CFCL – LF: 0.067 (dry gas) + 0.073 (steam); HF: 0.127 (dry gas) + 0.139 (steam).

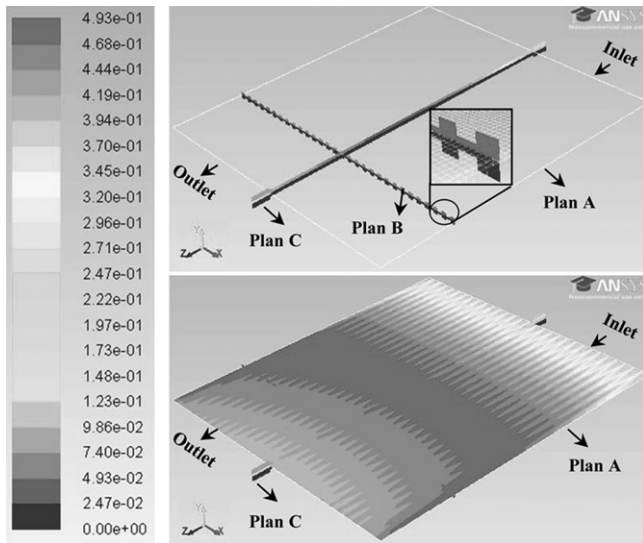


Fig. 6. Schematic view of different spatial axes on a 3D contour of hydrogen molar fraction.

does not reach the equilibrium. Another aspect to consider is the differences in concentration and temperature from both kinetic-based models which then lead to differences in the rates of physical processes both within the anode and in the external channels. In fact, all previous kinetic models have been developed and validated with experimental test data under specific operating conditions. Therefore, depending on the operating conditions, choosing the right correlation for the reforming reaction rate can affect the predicted results significantly.

Furthermore, a comparison of the predicted $V-I$ curves and experimental data under different operating conditions is shown in

Fig. 5. It is worth mentioning that all experimental data has been reported by Ceramic Fuel Cell Ltd. (CFCL) and from the similar geometry considered in this study. It was observed that the prediction of the polarization curves from 3D CFD model (case 3) exhibit good agreement with the experimental data. However, similar to the work of Xia et al. [10] and considering that the variation of the ADL microstructural parameters have been investigated in this study, to accelerate the converged solution, the anode and cathode exchange current densities were considered as the constant fitting parameters to that of the experimental data, 3200 and 1800 A m^{-2} respectively. In addition, there are uncertainties within some input parameters which have been extracted from the open literature [4,13,36]. In view of this, it is expected that some amount of discrepancies between the predicted results and experimental data will be observed as discovered at the low current densities with higher flow and temperature conditions. However, considering the purpose of this work for parametric study of the combined effects of the flow field design and ADL micro structural parameters on the cell overall performance, the validation goal is not to precisely fit the experimental data, but rather to capture their overall trend. In view of this, the numerical simulation of cases two and three were repeated for different structural parameters of the anode diffusion layer. The model predictions are mapped out along different spatial axes. As it is shown in Fig. 6, the dimensionless width and length represent the distances from intersection of plan A with B at 90% length and, plan A with C at 50% width of the cell respectively. In addition, to show the variation of the components' molar fractions and the reactions involved in the process, plan A has been projected along y -direction (the cell thickness) and in different computational domains, from catalyst layers to gas channels.

7.2. Effects of the ADL porosity

For parametric analysis the effect of the ADL porosity, case 2 and case 3 under low flow condition with pore size of $4.4 \mu\text{m}$ and the

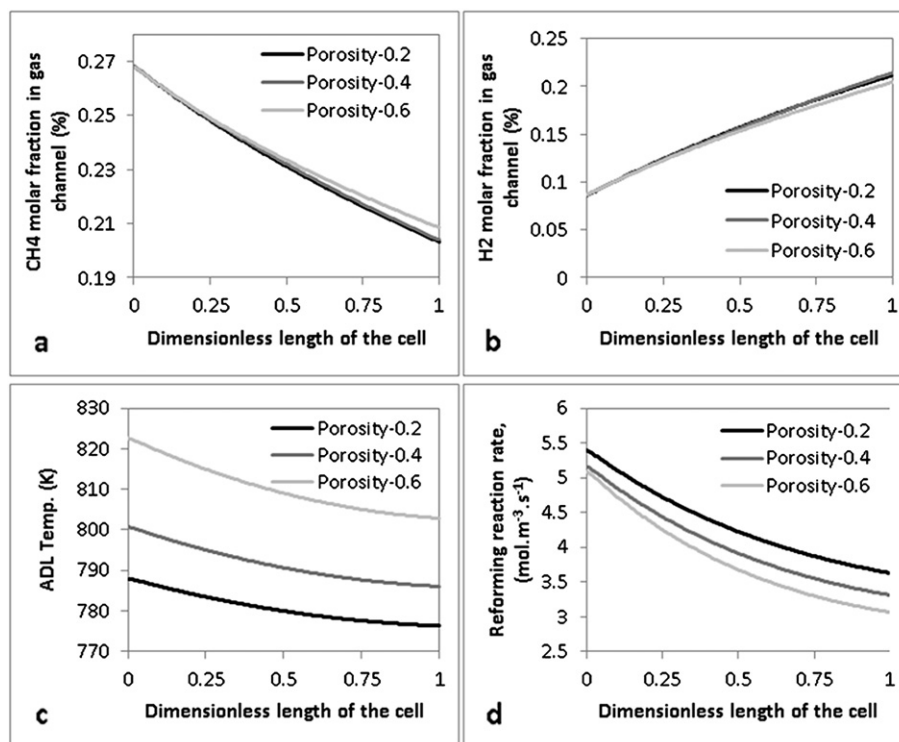


Fig. 7. Simulation results for the effects of porosity along the length of the cell – (case 2).

ADL thickness of 200 μm are investigated as follows. Fig. 7 illustrates the simulation results of case 2 for different porosity of the anode diffusion layer along the length of the cell. As shown here, without considering the electrochemical reaction and thermal effect of the air flow, temperature drop and reforming reaction rate increase while porosity varies from 0.6 to 0.2. However, under the effect of different porosities and within the initial length of the cell, the differences between the reforming reaction rates are less significant. Furthermore, distributions of methane and hydrogen molar fractions are quite similar for the porosities of 0.2 and 0.4. The results may come from the combined effects of porosity on effective diffusion and catalytic surface area. On the one hand, increasing the electrode porosity promotes the influence of the gas inlet operating conditions and components' diffusion through the porous media. On the other hand, increasing the electrode porosity means less reactive surface area that is predominant for decreasing the reforming reaction rate. Furthermore, distribution of the key parameters along other spatial paths provides better understanding for the combined effects of geometrical factors and micro-structural parameters on transport phenomena within the cell. As shown in Fig. 8, molar fraction of methane is lower for the mid channels. However, under the same velocity profile that comes from the effect of the flow field design, decreasing of the ADL porosity intensifies methane conversion within the mid channels. This observation reveals the complex interaction between the anode flow field design and ADL micro-structural parameters.

In short, under the effects of the geometrical factors and catalytic chemical reactions, porosity of 0.4 seems to be more appropriate for promoting methane conversion with lower temperature drop. However, to obtain the optimum value of porosity, we need to include the heat effects from the air channels and do a trade-off between the influences of chemical and electrochemical reactions. In this regard, Fig. 9 shows the simulation results of case 3 to picture the effects of porosity on distribution of the key parameters along the length of the cell. In Fig. 9, it is clearly shown that decreasing porosity hinders multicomponent gas transport and consequently increases differences of the components' molar fractions between the anode diffusion layer and gas channels (cf. – Fig. 9a, b, g and h). Although at a porosity of 0.2 less methane diffuses through the anode diffusion layer, stimulating heat effects of the air flow and electrochemical reaction rate in addition to availability of more reactive surface area counterbalance the ADL diffusional resistance to promote the reforming reaction rate (Fig. 9d). Furthermore, as it is shown in Fig. 9c, decreasing of porosity affects distribution of the current density and causes the location of the maximum current tends to shift towards the inlet regions of the cell. This observation underlines the complex interplay between the reforming and electrochemical reaction rates on distribution of fields. Temperature profiles of case 3 are illustrated in Fig. 9e. In contrast with case 2, the cooling effect of the reforming reaction is compensated with the heat effects from the air flow and electrochemical reaction rate. As the results, an increasing trend of temperature is presented along the length of the cell. In addition, at porosity of 0.2, temperature drop is effectively decreased within the small length of the inlet regions that consequently can improve thermal stability of the cell components. In fact, the internal reforming reaction consumes net heat and the electrochemical reactions generate heat globally. As it was shown in Fig. 9f and i, distribution of the activation and ohmic overpotentials are consistent with temperature and current density. It can also be recognized from Fig. 9f, that small changes in the anode activation overpotential can result in relatively large changes in current density. This is due to the exponential correlation between these two.

Furthermore, as it is shown in Fig. 10, including effects from the electrochemical reaction rate and comparing with simulation results of case 2, distribution of hydrogen along the width of the cell comes

into different view. This observation can be explained by the dominant influence of the electrochemical reaction rate on consumption of hydrogen over the effect of the catalytic reforming on hydrogen yield.

However, similar to the simulation results of case 2, under the combined effects of the anode flow field design and micro-structural parameters of the anode diffusion layer, decreasing of porosity causes further variation in distribution of different parameters along the width of the cell. However, this variation is not significant while decreasing of porosity causes less temperature drop and more uniform distribution of temperature and current density along the length of the cell. In view of this, porosity of 0.2 is beneficial for the overall performance of the cell. In fact, an optimum porosity that results in the best performance of methane conversion will not result in the improved SOFC performance.

7.3. Effects of the ADL pore size

For parametric analysis the effect of the ADL pore size, case2 and case3 under low flow condition with porosity of 0.4 and the ADL thickness of 200 μm are investigated as follows. Fig. 11 illustrates the simulation results of case 2 for analysing the effects of the pore radius on distribution of the key parameters along the length of the cell. Similar to the results reflecting the effect of the electrode porosity, as the pore size decreases, the reforming reaction rate increases and the smallest pore size is beneficial to that. However, unlike the effects of porosity, variation of the pore size has intensive effects on components' diffusional resistance, reforming reaction rate and temperature drop. Furthermore, distribution of the key parameters along the width of the cell (Fig. 12), gives another evidence for the predominant effects of the ADL pore size on reactive surface area and consequently on the reforming reaction rate in regions with higher residence time.

Fig. 13 shows the simulation results of case 3 to analyse the effects of the pore radius on the overall performance and distribution of different parameters along the length of the cell. In this regard, it is interesting to mention that apart from the initial length of the cell, the maximum reforming reaction rate and consequently, the maximum hydrogen yield correspond to the pore size of 2.4 μm which is in middle of the pore size range. This observation can be justified by two different mechanisms governing the molar fraction of hydrogen at a given operating conditions: (1) H_2 production due to the reforming and water gas shift reactions and (2) resistance of the porous anode to H_2 diffusion. As shown in Fig. 13, decreasing the pore size causes the reactants' diffusional resistance and consequently the differences of the reactants' molar fractions between the anode diffusion layer and gas channels to be significantly increased (please refer to Fig. 13a, b, g and h). As a result, not only the multi component gas transport but also the current density is significantly influenced. In other words, within the initial length of the cell and for the smallest pore size, the anode diffusion layer is less influenced by the fuel inlet operating condition and the hydrogen produced from the reforming reaction effectively promotes the electrochemical reaction rate (Fig. 13c). However, except for the initial distance of the cell, hydrogen diffusion from gas channels to the reactive surface area of the anode catalyst layer become critical.

Thus considering substantial components' diffusional resistance of the smallest pore size, the cell overall performance decreases significantly. Moreover, under the combined effects of the reforming and electrochemical reaction rates, the mid-range of the pore size results in less temperature drop while the smallest pore size causes the fuel gas temperature to be decreased considerably. It can also be observed from Fig. 13f and i, that distribution of the overpotentials are consistent with the current density and temperature profiles.

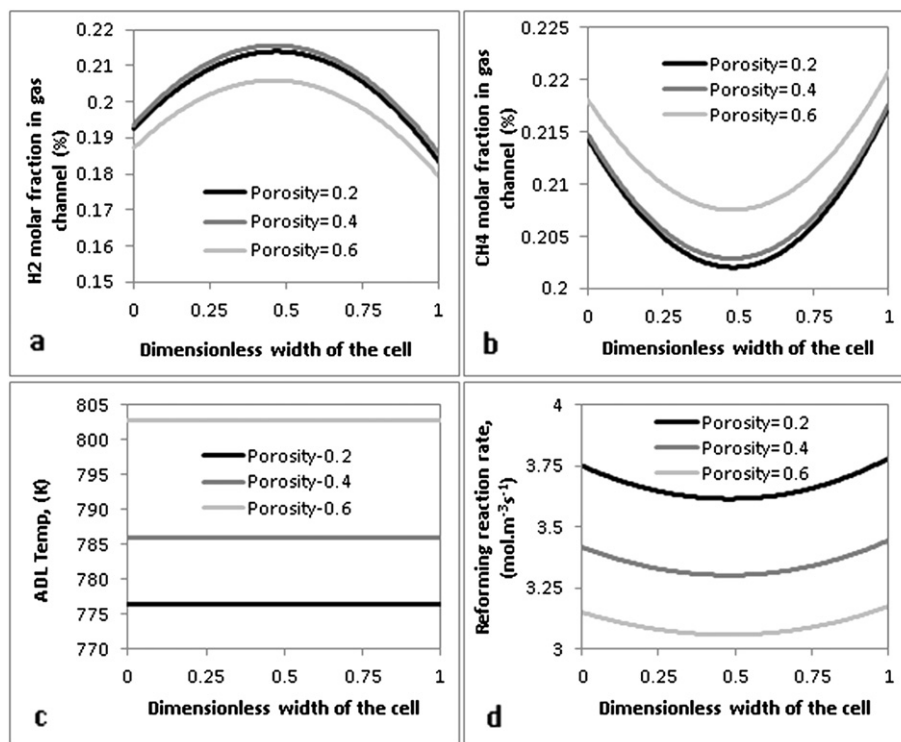


Fig. 8. Simulation results for the effects of porosity along the width of the cell – (case 2).

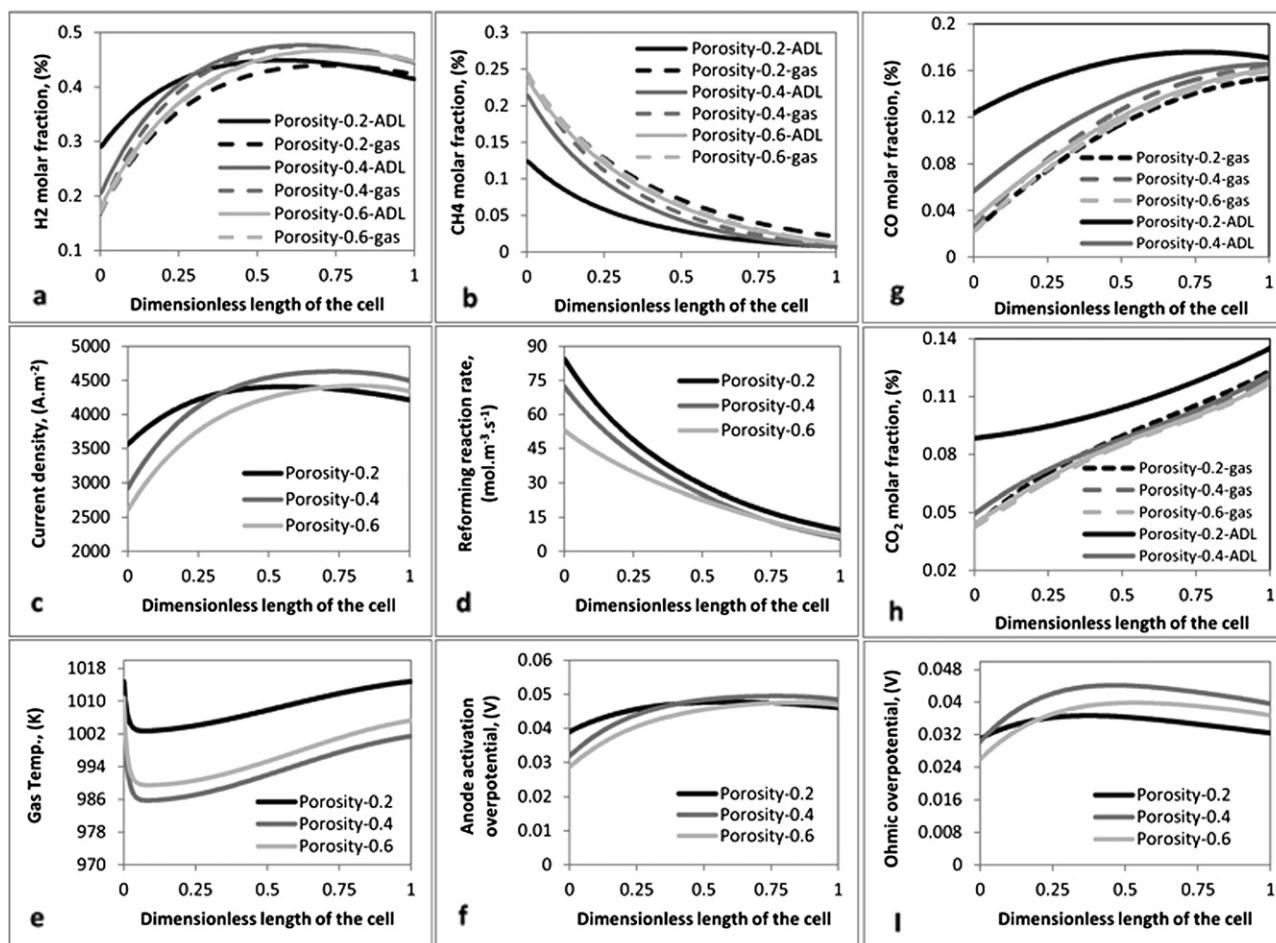


Fig. 9. Simulation results for the effects of porosity along the length of the cell (case 3 at 0.819 V).

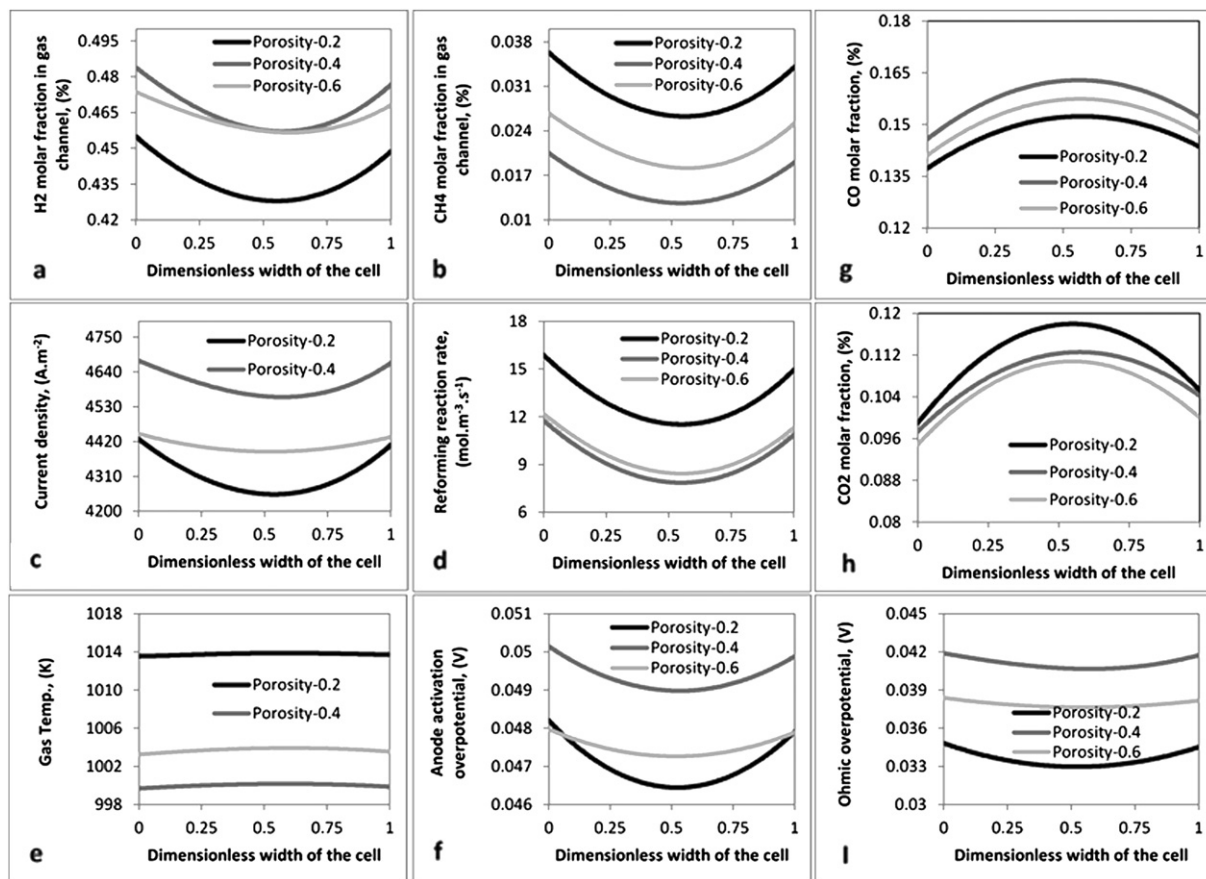


Fig. 10. Simulation results for the effects of porosity along the width of the cell (case 3 at 0.819 V).

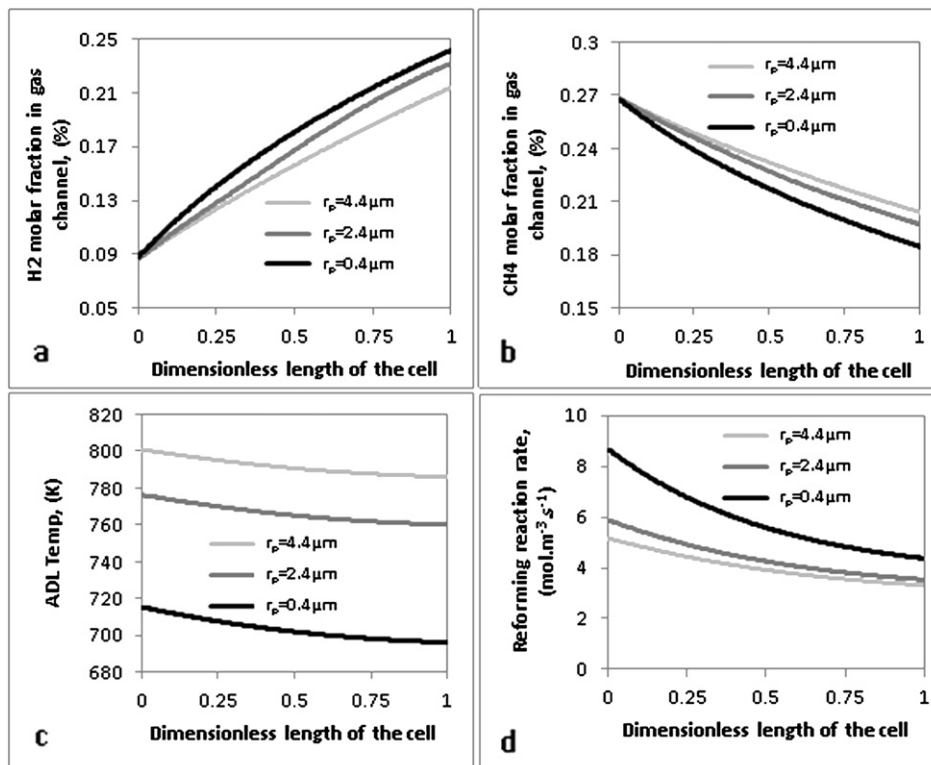


Fig. 11. Simulation results for the effects of pore size along the length of the cell (case 2).

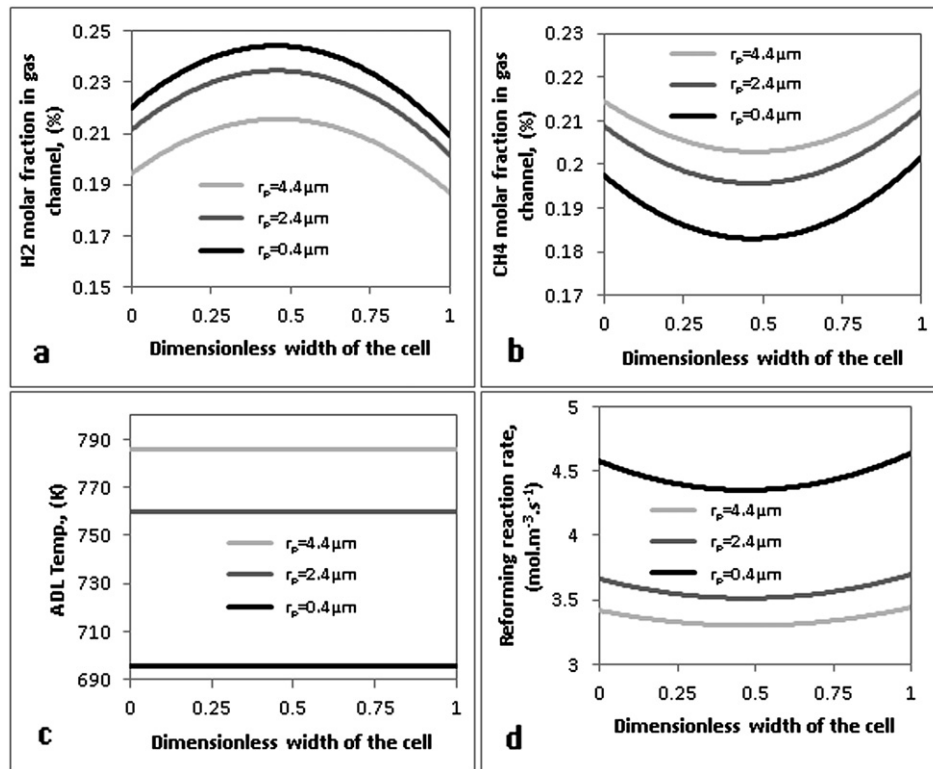


Fig. 12. Simulation results for the effects of pore size along the width of the cell (case 2).

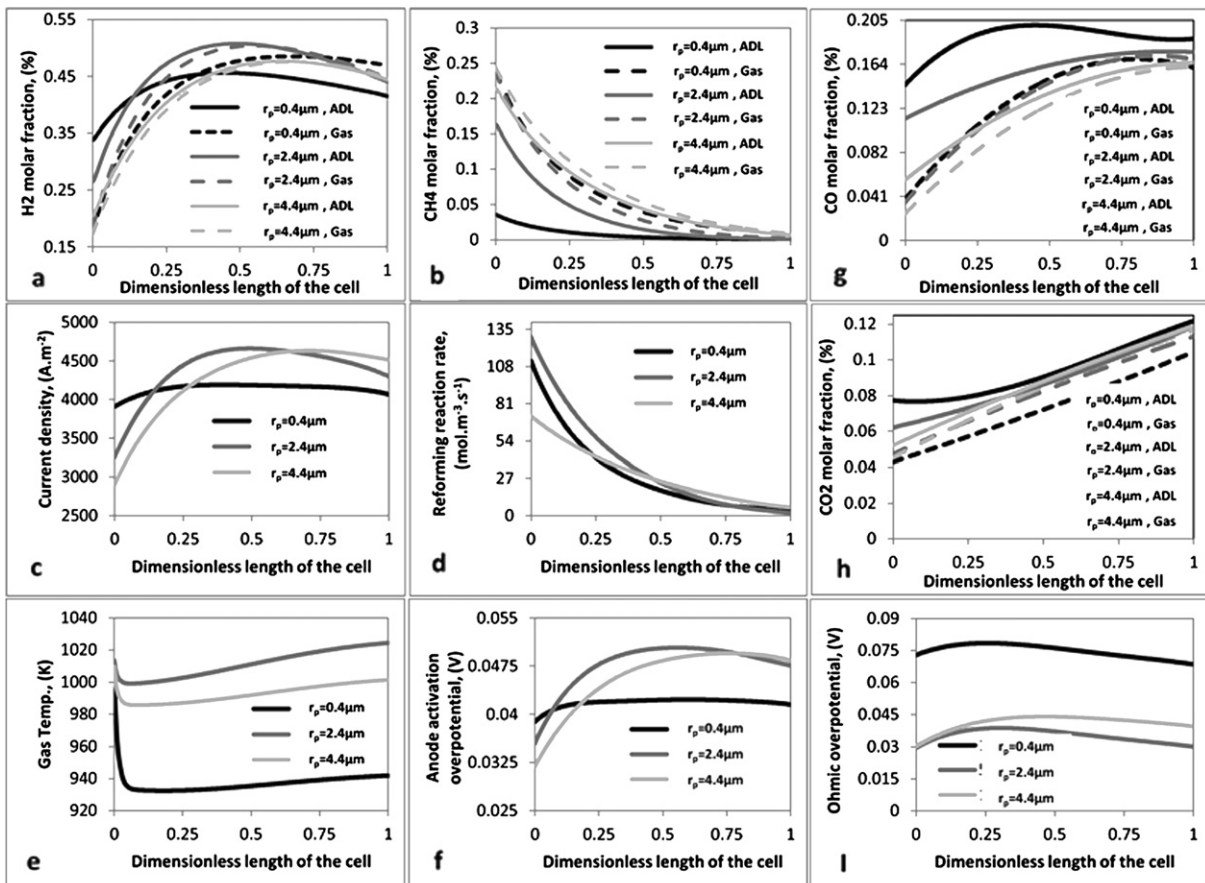


Fig. 13. Simulation results for the effects of pore size along the length of the cell (case 3 at 0.819 V).

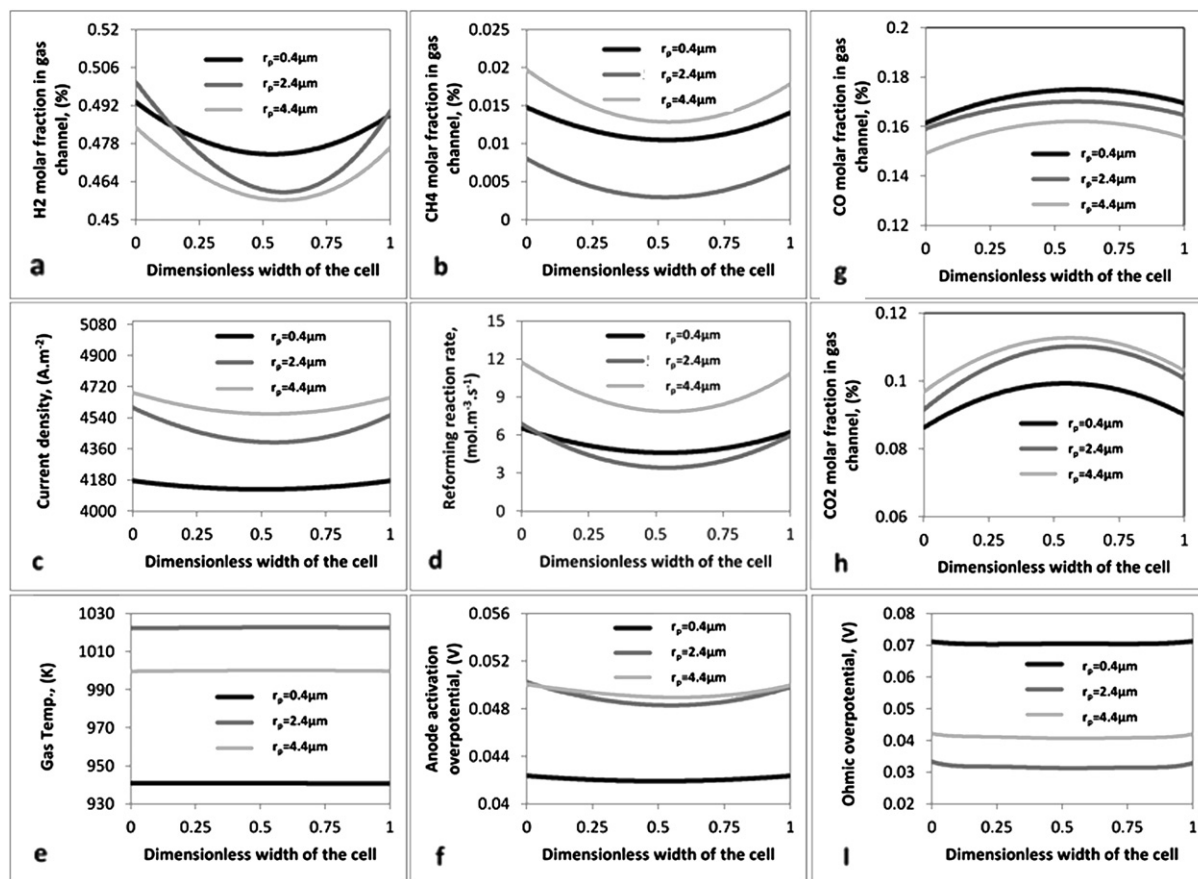


Fig. 14. Simulation results for the effects of pore size along the width of the cell (case 3 at 0.819 V).

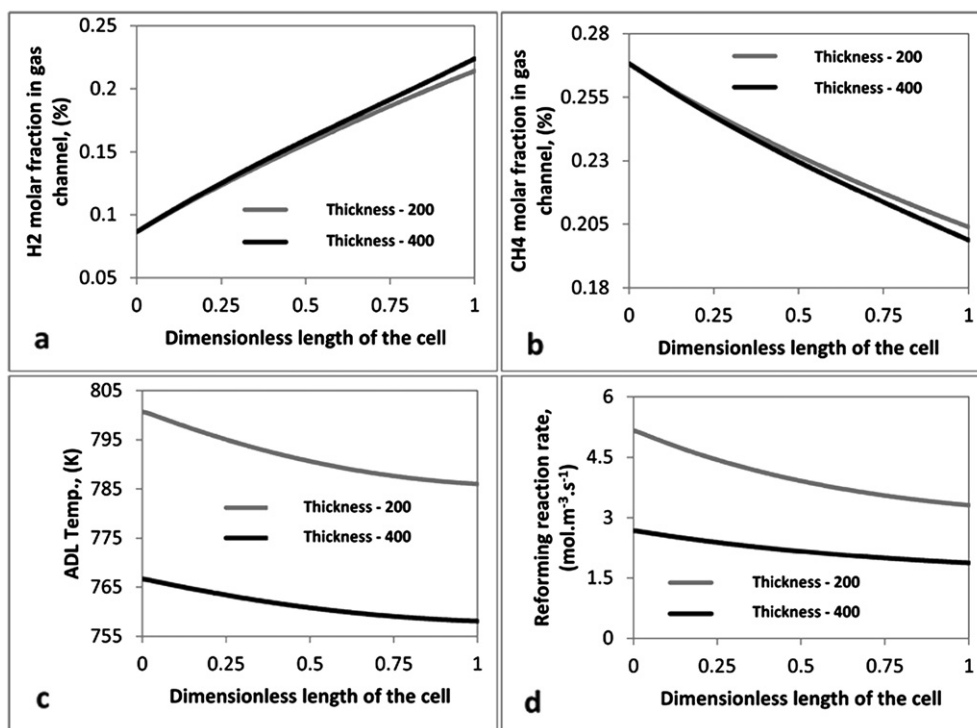


Fig. 15. Simulation results for the effects of ADL thickness along the width of the cell (case 2).

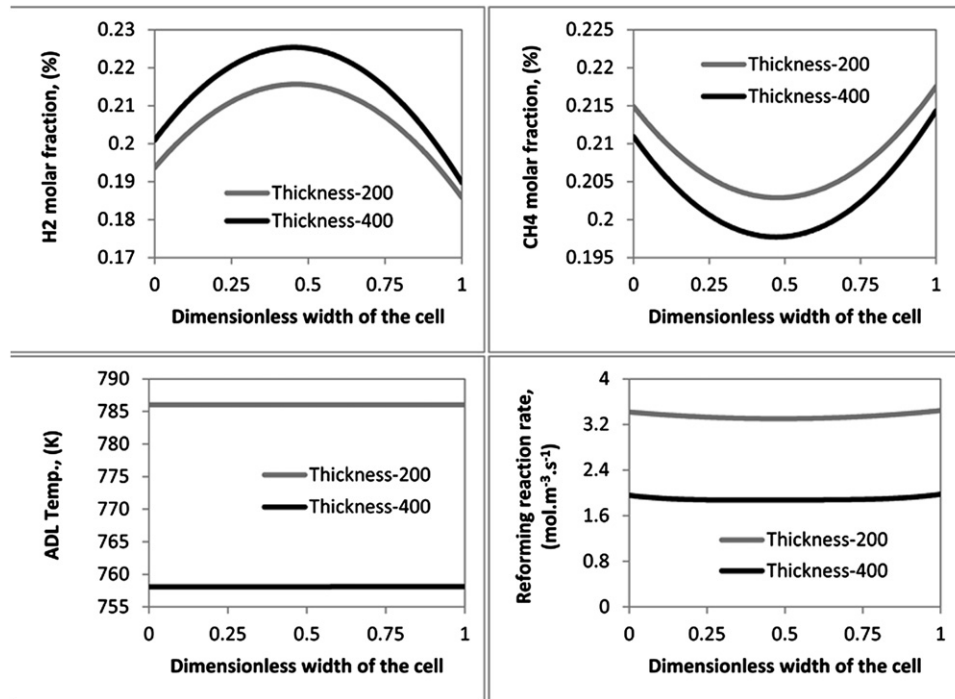


Fig. 16. Simulation results for the effects of ADL thickness length the width of the cell (case 2).

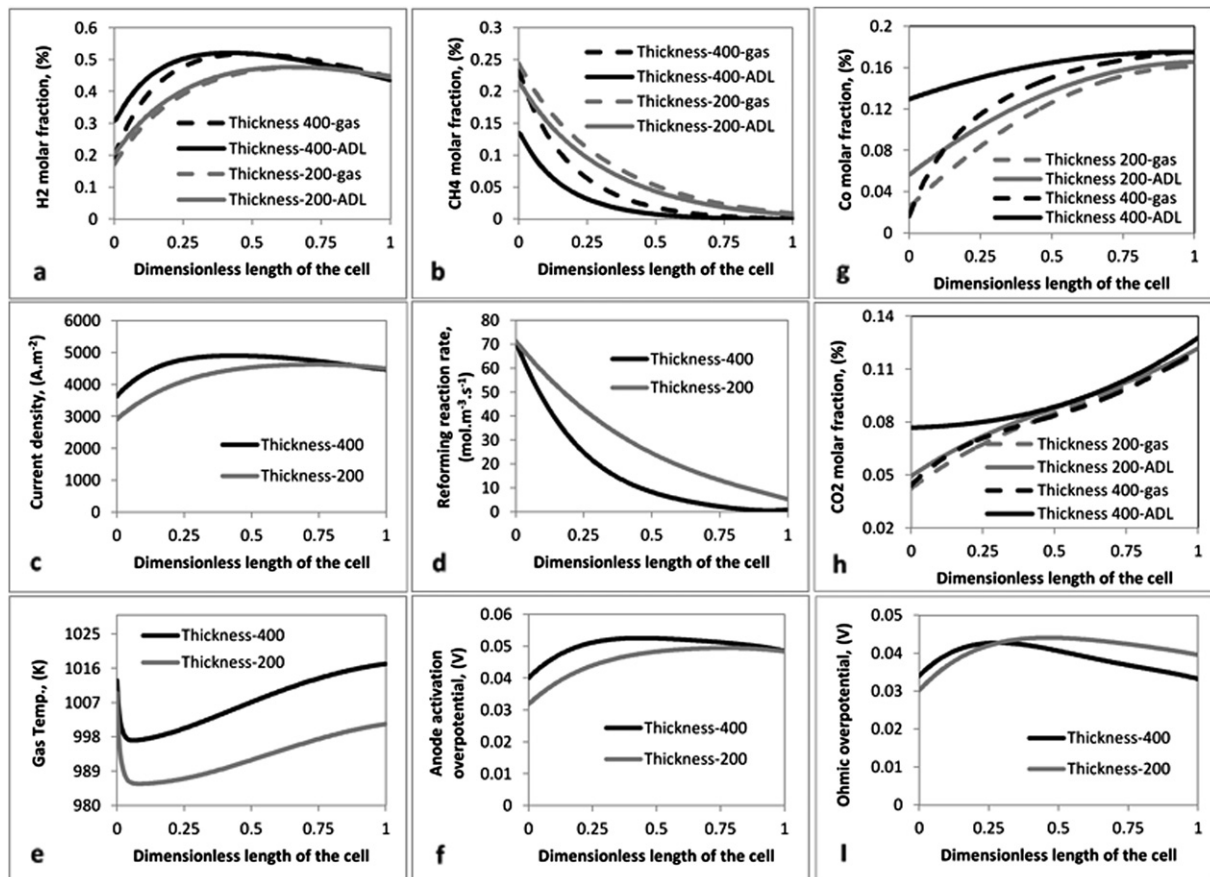


Fig. 17. Simulation results for the effects of ADL thickness along the length of the cell (case 3 at 0.819 V).

As the result, although the mid-range of the pore size exhibits further variation in distribution of different parameters across the width of the cell (Fig. 14), considering the operational condition and comparing with distribution of the same parameters along the length of the cell, this variant is relinquished. In fact, in contrast to the conclusion from the simulation results of case 2, under the influences of the electrochemical reaction rate and heat effects of the air channels, the midrange of the pore size is the most appropriate for engineering of the anode diffusion layer.

7.4. Effects of the ADL thickness

The effects of the ADL thickness on the SOFC performance are another parameter that needs to be investigated. In this regard, case 2 and case 3 under low flow condition with porosity of 0.4 and the ADL pore size of $4.4\ \mu\text{m}$ are investigated as follows. As shown in Figs. 15 and 16, temperature drop and methane conversion are found to be increased with increasing the ADL thickness. It is consistent with the fact that increasing the ADL thickness provides sufficient number of the catalytic sites required for the methane reforming. However, at the same position within the anode diffusion layer closing to the anode catalyst layer, increasing of the ADL thickness causes the reforming reaction rate to be decreased and its distribution along the length of the cell becomes less intensive (Fig. 15d). This is due to the combined effects of the species diffusional resistance and dilution of methane with the hydrogen product. It is worth mentioning that increasing the ADL thickness increases reactants' diffusional path, which in turn increases the resistance to the diffusional mass transfer. In addition,

as shown in Fig. 15, distribution of different parameters along the width of the cell reveals the intensive effect of the increased ADL thickness on methane conversion in mid channels. On the other hand, for the mid channels with higher residence time, although the diffusional path increased; however, further catalytic reaction sites can be involved in the reforming reaction, which in turn causes further methane conversion.

Finally, the simulation results of case 3 including the influences of the ADL thickness, electrochemical reaction and heat effects of the air channels are given in Figs. 17 and 18. In this regard, hydrogen molar fraction increased within the initial length of the cell followed by gradual decrease that is controlled by the combined effects of diffusional resistance, reforming and electrochemical reaction rates (Fig. 17a). Furthermore, increasing of the ADL thickness affects the differences of hydrogen and methane concentrations between the anode diffusion layer and gas channels, which in turn intensify decreasing of the reforming reaction rate (Fig. 17d). However, as it is shown in Fig. 17a and b, with respect to the availability of further reaction sites for the reforming reaction rate, methane conversion and hydrogen yield were increased. It consequently promotes the electrochemical reaction and results in less temperature drop. This observation is more noticeable within the initial length of the cell, due to the direction of the hydrogen mass transfer that is quite opposite to the rest of the cell. Additionally, increasing the ADL thickness increases the hydrogen residence time at the anode catalyst layer and causes further improvement of the SOFC performance. Under the effects of the ADL thickness on reforming reaction and the electrochemical performance, temperature drop and ohmic overpotential improved as well. Finally, as it

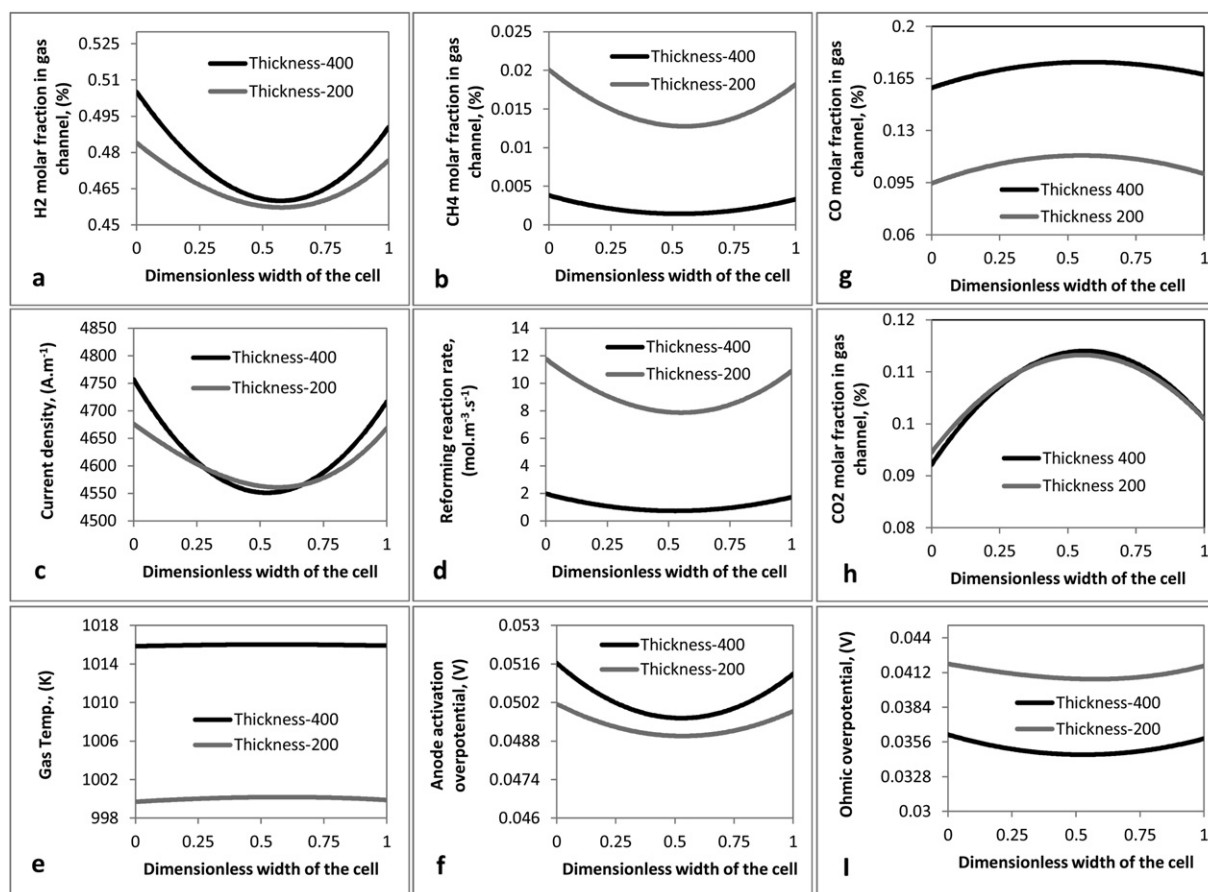


Fig. 18. Simulation results for the effects of ADL thickness along the width of the cell (case 3 at 0.819 V).

Table 7

- Single cell stack simulation results (cell voltage = 0.819 V).

Case 3 – Effect of the ADL porosity (pore size: 4.4 μm & thickness: 200 μm)						
Porosity	OCV	i_{avg}	η_{act}^A	$ \eta_{act}^C $	$\eta_{ohm}(i \times R_{ohm})$	T_{avg}
0.2	0.995	4483.96	0.04869	0.0907	0.0364	1009
0.4	0.99861	4472.8	0.047844	0.089192	0.0424	990
0.6	0.9914	4301.06	0.04632	0.08683	0.0392	997
Case 3 – Effect of the ADL pore size (porosity of 0.4 & thickness of 200 μm)						
Pore size, μm	OCV	i_{avg}	η_{act}^A	$ \eta_{act}^C $	$\eta_{ohm}(i \times R_{ohm})$	T_{avg}
4.4	0.99861	4472.8	0.047844	0.089192	0.0424	990
2.4	1.00073	4680.93	0.0508	0.094	0.0366	1013
0.4	1.02281	4471.4	0.04544	0.08477	0.0734	944
Case 3 – Effect of the ADL thickness (porosity of 0.4 & pore size: 4.4 μm)						
Thickness, μm	OCV	i_{avg}	η_{act}^A	$ \eta_{act}^C $	$\eta_{ohm}(i \times R_{ohm})$	T_{avg}
200	0.99861	4472.8	0.047844	0.089192	0.0424	990
400	1.00423	4656.9	0.051330	0.094778	0.0389	1004

is shown in Fig. 18, distribution of the key parameters along the width of the cell is another evidence for the combined effects of the anode flow field design and ADL micro-structural parameters on distribution of fields.

Consistent with the simulation results of case 3, and to get an easier understanding for an optimal set of the ADL microstructure, average temperature, current density, OCV and overpotentials for different porosity, pore size and thicknesses are listed in Table 7. In comparison with case2, it is clear that the ADL microstructure that promotes the reforming reaction rate will not automatically improve the SOFC performance.

8. Conclusions

A CFD approach was implemented to analyse the combined effects of the flow field design and micro structural parameters of the anode diffusion layer on each the reactions involved in the process. Evaluation of the results shows that 3D model is more representative of the global reforming reaction rate while the predicted $V-I$ curves exhibit good agreement with the experimental data that was reported from the same geometry. In addition, control volume treatment of the electrodes creates a detailed framework for accurate justification of different behaviour. In this regard, it was shown that the complex interaction between macro and micro structural parameters can effectively influence distribution of the key parameters along different spatial domains. However, variation of the ADL microstructures has different intensity effects on multi component gas transport and the reactions involved in the process. Furthermore, an optimal set of the ADL microstructure, which can effectively promote the reforming reaction rate, will not automatically result in improved SOFC performance. In this regard, the ADL structure with the porosity of 0.4 and 0.2 is beneficial for the reforming and electrochemical reactions, respectively. In addition, similar to the results reflecting the effect of porosity, the pore size of 0.4 and 2.4 μm result in the best performance for each of the reactions correspondingly. However, unlike the effects of porosity, variation of the pore size has intensive effects on components' diffusional resistance, reaction rates and temperature drop. Furthermore, it was shown that increasing the ADL thickness increases the hydrogen residence at the neighbouring anode catalyst layer and affects the SOFC performance predominantly within the initial length of the cell. Nevertheless, it can reduce the reforming reaction rate due to dilution of the reactants with the hydrogen product. The developed model is a powerful tool to study complex fuel cell related problems

and to optimize fuel cells' structure. Additionally, the numerical simulation results of this model can provide useful information for evaluation of the results from our previous SOFC tank in series model [43] and also grading of the microstructural properties of the anode diffusion layer which can effectively improve the SOFC performance. However, in spite of developing an innovative technique to reduce the computational time, application of the multi core parallel processing is a fundamental aspect that must be taken into account in our future study especially to model of a number of cells arranged in a single stack.

Acknowledgement

The first author gratefully acknowledges Curtin University for the CSIRS Scholarship. The authors are also grateful the Australian Research Council (ARC) for Grant DP0880483 and to Ceramic Fuel Cells Company for their helpful suggestions and for providing experimental data of similar SOFC stacks.

Appendix A. Estimation of the gas diffusivity

The binary diffusivity of a pair of gaseous species i and j is modelled by the Fuller's correlation [44].

$$D_{ij} = \frac{1.013^{-2} T^{1.75} \left(\frac{1}{M_{w,i}} + \frac{1}{M_{w,j}} \right)^{0.5}}{P \left[(\sum v_i)^{1/3} + (\sum v_j)^{1/3} \right]^2} \quad (A-1)$$

However, diffusion coefficient of species i in the multi-component gas mixture is calculated by the expression that is based on the binary coefficients [11].

$$D_{i,GM} = \frac{1 - y_i}{\sum_{j \neq i}^m \frac{y_j}{D_{ij}}} \quad (A-2)$$

For the porous layer with large pores, diffusion flux is predominant and the effective diffusion coefficient components can be calculated from Eq. (A-2). However, Knudsen diffusion occurs in the porous layer with small pores when the mean free-path of molecules is smaller than the pore size, and the molecules collide with the walls more often between themselves. Knudsen diffusion coefficient $D_{i,k}$ is calculated based on the free molecule flow theory [45].

$$D_{i,k} = \frac{2}{3} r_p \sqrt{\frac{8RT}{\pi M_{w,i}}} \quad (A-3)$$

To account for the effects of Knudsen diffusion, porosity and the increased diffusion length due to the tortuous paths of real pores of the porous electrodes, the effective diffusion coefficient can be evaluated as follows [45].

$$D_i^{\text{eff}} = \frac{\varepsilon}{\tau} \left(\frac{D_{i,GM} \times D_{i,k}}{D_{i,GM} + D_{i,k}} \right) \quad (A-4)$$

Nomenclature

A_s	reactive surface area per unit volume (m^{-1})
d_p	particle diameter (m)
D_i^{eff}	effective diffusion coefficients of the species ($\text{m}^2 \text{s}^{-1}$)
E	specific energy (J kg^{-1})
E_{cell}	cell voltage (V)

E_{act}	activation energy (J mol^{-1})
F	Faraday's constant ($96,485 \text{ C mol}^{-1}$)
ΔG^0	standard Gibbs free energy change (J mol^{-1})
ΔH	enthalpy change of reaction (J mol^{-1})
h	enthalpy (J mol^{-1})
i	current density (A m^{-2})
i_{avg}	average current density (A m^{-2})
i_0	exchange current density (A m^{-2})
J	diffusion flux ($\text{mol m}^{-2} \text{ s}^{-1}$)
ℓ	thickness (μm)
M_w	molecular weight (g mol^{-1})
n_e	number of electrons participating in electrochemical reaction
n_t	total number of particles per reaction volume (m^{-3})
n_{elde}	number fraction of electrode particles in the anode functional layers (%)
n_{elyt}	number fraction of electrolyte particles in the anode functional layers (%)
P	pressure (Pa)
P_{elde}	probability of the electrode particles
P_{elyt}	probability of the electrolyte particles
r_{elde}	radius of electrode particles
r_{elyt}	radius of electrolyte particles
r_p	pore radius
R	ideal gas constant ($\text{J mol}^{-1} \text{ K}^{-1}$)
S_h	volumetric heat source term ($\text{J m}^{-3} \text{ s}^{-1}$)
S^r	volumetric mass source term ($\text{mol m}^{-3} \text{ s}^{-1}$)
S_M	momentum source term (N m^{-3})
T	temperature (K)
T_{avg}	average temperature (K)
t	time (s)
\vec{u}	tensor of velocity (m s^{-1})
y	species mole fraction (%)
Z	average coordinate number
Z_{elde}	coordinate number of the electrode particles
Z_{elyt}	coordinate number of the electrolyte particles

Greek letters

α_p	permeability (m^2)
ε	porosity (%)
η_{act}	activation overpotential of the electrodes (V)
θ	contact angle ($^\circ$)
ι	tortuosity
κ	reaction rate constant
μ	dynamic viscosity (Pa s)
ν_i	species stoichiometric coefficient
ρ	density (mole m^{-3})
∂	conductivity (S/m)
τ	viscous stress (Pa)
ψ_{elde}	volume fraction of the electrode particles (%)
ψ_{elyt}	volume fraction of the electrolyte particles (%)

Acronyms – sub/superscripts

ADL	anode diffusion layer
ACL	anode catalyst layer
A	anode electrode
C	cathode electrode
cell	cell
CDL	cathode diffusion layer
CCL	cathode catalyst layer
chem	chemical reaction
cat	catalyst layer

elde	electrode
elec	electrochemical reaction
eff	effective
eq	equilibrium
elyt	electrolyte
f	fuel gas channel – forward reaction
HF	high flow rate
i	species i
LF	low flow rate
s	solid phase
SMR	steam methane reforming
WGS	water gas shift

References

- [1] A. Arpornwichanop, N. Chalermpanchai, Y. Patcharavorachot, S. Assabumrungrat, M. Tade, Int. J. Hydrogen Energy 34 (2009) 7780–7788.
- [2] E. Fontell, T. Kivisaari, N. Christiansen, J.B. Hansen, J. Pålsson, J. Power Sources 131 (2004) 49–56.
- [3] K.P. Recknagle, R.E. Williford, L.A. Chick, D.R. Rector, M.A. Khaleel, J. Power Sources 113 (2003) 109–114.
- [4] Y. Yang, X. Du, L. Yang, Y. Huang, H. Xian, Appl. Therm. Eng. 29 (2009) 1106–1113.
- [5] M. Hussain, X. Li, I. Dincer, J. Power Sources 189 (2009) 916–928.
- [6] S. Hosseini, M.O. Tade, K. Ahmed, CHEMECA 2011: Engineering a Better World: Sydney Hilton Hotel, NSW, Australia, 18–21 September 2011, (2011) 1514.
- [7] P. Aguiar, C. Adjiman, N.P. Brandon, J. Power Sources 138 (2004) 120–136.
- [8] N. Autissier, D. Larrain, D. Favrat, J. Power Sources 131 (2004) 313–319.
- [9] V.A. Danilov, M.O. Tade, Int. J. Hydrogen Energy 34 (2009) 8998–9006.
- [10] W. Xia, Y. Yang, Q. Wang, J. Power Sources 194 (2009) 886–898.
- [11] H. Yakabe, M. Hishinuma, M. Uratani, Y. Matsuzaki, I. Yasuda, J. Power Sources 86 (2000) 423–431.
- [12] J. Yuan, Chem. Prod. Process Model. 5 (2010) 12.
- [13] M. Hussain, X. Li, I. Dincer, J. Power Sources 161 (2006) 1012–1022.
- [14] M. Hussain, X. Li, I. Dincer, Int. J. Energy Res. 29 (2005) 1083–1101.
- [15] C. Huang, S. Shy, C. Chien, C. Lee, J. Power Sources 195 (2010) 2260–2265.
- [16] J. Shi, X. Xue, Electrochim. Acta 55 (2010) 5263–5273.
- [17] J. Shi, X. Xue, Chem. Eng. J. 182 (2012) 607–613.
- [18] M. Andersson, J. Yuan, B. Sundén, Int. J. Heat Mass Transfer (2011).
- [19] A. Abbaspour, J.L. Luo, K. Nandakumar, Electrochim. Acta 55 (2010) 3944–3950.
- [20] D.H. Jeon, Electrochim. Acta 54 (2009) 2727–2736.
- [21] Y. Shi, N. Cai, C. Li, C. Bao, E. Croiset, J. Qian, Q. Hu, S. Wang, J. Power Sources 172 (2007) 235–245.
- [22] Z. Qu, P. Aravind, S. Boksteen, N. Dekker, A. Janssen, N. Woudstra, A. Verkooijen, Int. J. Hydrogen Energy 36 (2011) 10209–10220.
- [23] P.W. Li, L. Schaefer, M.K. Chyu, J. Heat Transfer 126 (2004) 219.
- [24] F. Lubelli, J. Eng. Gas Turbines Power 122 (2000) 27.
- [25] S. Campanari, P. Iora, Fuel Cells 5 (2005) 34–51.
- [26] K. Ahmed, K. Foger, Catal. Today 63 (2000) 479–487.
- [27] J. Yuan, Y. Huang, B. Sundén, W.G. Wang, Heat Mass Transfer 45 (2009) 471–484.
- [28] M. Ni, D.Y.C. Leung, M.K.H. Leung, J. Power Sources 183 (2008) 133–142.
- [29] J.M. Klein, Y. Bultel, S. Georges, M. Pons, Chem. Eng. Sci. 62 (2007) 1636–1649.
- [30] P. Hofmann, K. Panopoulos, L. Fryda, E. Kakaras, Energy 34 (2009) 2151–2157.
- [31] B. Haberman, J. Young, Int. J. Heat Mass Transfer 47 (2004) 3617–3629.
- [32] I. Drescher, W. Lehnert, J. Meusinger, Electrochim. Acta 43 (1998) 3059–3068.
- [33] K. Hou, R. Hughes, Chem. Eng. J. 82 (2001) 311–328.
- [34] Z. Qu, P. Aravind, N. Dekker, A. Janssen, N. Woudstra, A. Verkooijen, J. Power Sources 195 (2010) 7787–7795.
- [35] A. Chaisantikulwat, C. Diaz-Goano, E. Meadows, Comp. Chem. Eng. 32 (2008) 2365–2381.
- [36] M. Ni, D.Y.C. Leung, M.K.H. Leung, Energy Convers. Manage. 50 (2009) 268–278.
- [37] H. Zhu, R.J. Kee, V.M. Janardhanan, O. Deutschmann, D.G. Goodwin, J. Electrochem. Soc. 152 (2005) A2427.
- [38] P. Costamagna, P. Costa, V. Antonucci, Electrochim. Acta 43 (1998) 375–394.
- [39] A. Bertei, C. Nicoletta, J. Power Sources (2011).
- [40] H.K. Versteeg, W. Malalasekera, An Introduction to Computational Fluid Dynamics: The Finite Volume Method, Pearson Education Limited, 2007.
- [41] E. Achenbach, E. Riensche, J. Power Sources 52 (1994) 283–288.
- [42] D. Green, R. Perry, Perry's Chemical Engineers' Handbook, eighth ed., McGraw-Hill Companies, Incorporated, 2007.
- [43] S. Hosseini, V.A. Danilov, P. Vijay, M.O. Tade, Ind. Eng. Chem. Res. (2011) 1056–1069.
- [44] Y. Qi, B. Huang, K.T. Chuang, J. Power Sources 150 (2005) 32–47.
- [45] J. Yuan, Chem. Prod. Process Model. 5 (2010).